







Small-angle scattering interferometry with neutron orbital angular momentum states

Received: 24 May 2024

Accepted: 20 November 2024

Published online: 30 December 2024

 Check for updates

Dusan Sarenac^{1,2}  , Melissa E. Henderson^{2,3,4}, Huseyin Ekinci^{2,3}, Charles W. Clark⁵ , David G. Cory^{2,6}, Lisa DeBeer-Schmitt⁴, Michael G. Huber⁷ , Owen Lailey^{2,3}, Jonathan S. White⁸, Kirill Zhernenkov⁹ & Dmitry A. Pushin^{2,3}  

Methods to prepare and characterize neutron helical waves carrying orbital angular momentum (OAM) were recently demonstrated at small-angle neutron scattering (SANS) facilities. These methods enable access to the neutron orbital degree of freedom which provides new avenues of exploration in fundamental science experiments as well as in material characterization applications. However, it remains a challenge to recover phase profiles from SANS measurements. We introduce and demonstrate a novel neutron interferometry technique for extracting phase information that is typically lost in SANS measurements. An array of reference beams, with complementary structured phase profiles, are put into a coherent superposition with the array of object beams, thereby manifesting the phase information in the far-field intensity profile. We demonstrate this by resolving petal-structure signatures of helical wave interference for the first time: an implementation of the long-sought recovery of phase information from small-angle scattering measurements.

Small-angle neutron scattering (SANS) is a versatile technique that is used to probe the nanoscale structure and dynamics of materials such as polymers, biomolecules, magnetic nanoparticles, porous media, and metal-organic frameworks^{1–7}. Applications of SANS include studying self-assembly, phase diagrams, interactions of soft matter systems, investigating the magnetic properties and functionalization of nanomaterials, and combining SANS with neutron imaging to access multiple length scales from micrometers to nanometers^{8–12}. SANS is complementary to other scattering methods, such as small-angle X-ray scattering (SAXS), and can benefit from the use of contrast variation and isotope labeling^{13–15}.

In a typical SANS measurement neutrons propagate for several meters after passing through the sample and its environment before

they are detected by a position-sensitive neutron detector. Phase information is sacrificed in detection since the far-field neutron intensity profile is proportional to the square modulus of the Fourier transform of the outgoing wave function. Recent work, inspired by computed tomography methods, examined phase recovery by employing multi-angle SANS measurements^{16,17}.

Developments in the production and detection of structured neutron waves^{18–26} offer new methods for material characterization^{26–30} that would be further enhanced by the retrieval of phase information in SANS. In general, structured wave generation relies on tailoring the transverse phase profile of the wavefront to induce non-trivial propagation characteristics such as orbital angular momentum (OAM), non-diffraction, and self-acceleration^{31–35}. For example, imprinting an

¹Department of Physics, University at Buffalo, State University of New York, Buffalo, NY, USA. ²Institute for Quantum Computing, University of Waterloo, Waterloo, ON, Canada. ³Department of Physics and Astronomy, University of Waterloo, Waterloo, ON, Canada. ⁴Neutron Scattering Division, Oak Ridge National Laboratory, Oak Ridge, TN, USA. ⁵Joint Quantum Institute, National Institute of Standards and Technology and University of Maryland, College Park, MD, USA. ⁶Department of Chemistry, University of Waterloo, Waterloo, ON, Canada. ⁷National Institute of Standards and Technology, Gaithersburg, MD, USA. ⁸Laboratory for Neutron Scattering and Imaging, PSI Center for Neutron and Muon Sciences, Villigen, Switzerland. ⁹Jülich Centre for Neutron Science at Heinz Maier-Leibnitz Zentrum, Garching, Germany. ✉ e-mail: dusansar@buffalo.edu; dmitry.pushin@uwaterloo.ca

azimuthal phase gradient upon the wave function prepares helical waves that carry OAM and display a doughnut-like intensity profile in the far-field^{36–38}.

To advance SANS techniques for disambiguating the phase profile of the wave function, we adopt concepts from neutron interferometry (NI) and holography^{19,39}. We create a coherent superposition of two beams, termed object and reference beams, according to holography terminology⁴⁰, thereby yielding observable interference amplitudes to reveal phase information in the far field. We demonstrate this method by observing the petal-structure interference between two helical beams that have been prepared using arrays of fork-dislocation phase gratings and whose transverse amplitude profile takes on a doughnut-like form with propagation.

Results

SANS interferometry with structured waves

A conventional Mach-Zehnder (MZ) perfect-crystal NI prepares a coherent superposition of two paths at its output, which provides the phase information through direct measurement of interference³⁹. A distinguishing factor from the standard optical MZ interferometer setups is that the neutron transverse coherence length is orders of magnitude smaller than the beam size. Therefore, the action of the MZ NI is applied to each neutron, and the observed intensity at the output is their incoherent sum.

A challenge arises to integrate interferometry methods and structured neutron waves as their transverse amplitude profiles significantly change with propagation. In order to maximize the

interference signal, the object beams and the reference beams of the NI need to spatially overlap at the detector plane, which is dependent on instrument resolution and coherence effects⁴¹. Ref. 25 introduced methods to prepare well-defined OAM states and showed how the amplitude of the neutron wave packets deviates away from their central phase singularity with increasing OAM value. As a result, the radius of the doughnut-like profile of the OAM = 3 (OAM = 7) states at the neutron camera was measured to be ≈ 3 cm (≈ 5 cm), which was significantly bigger than the measured half-width half maximum, ≈ 1 cm, of the OAM = 0 state.

One way to achieve an appreciable overlap between the reference beams and the object beams is to utilize reference beams that possess complementary spatial phase profiles resulting in similar time-dependent amplitude profiles. In the case of the OAM preparation methods of ref. 25, this entails creating a coherent superposition between ℓ and $-\ell$ OAM states in each diffraction order, as shown in Fig. 1a. The intensity at the camera would take on the form of the well-known petal structure indicative of the OAM⁴², while the OAM dependent phase shift between the two beams would cause the petal profile to rotate. The general concept is shown in Fig. 1b where we consider two complementary arrays of fork-dislocation phase-gratings with periodicity a and separation distance d . The interference at the detector is achieved by ensuring that the phase profile of the reference beams $\phi_R(x, y)$ and the object beams $\phi_O(x, y)$ possess matching carrier wave vector k_x and complementary structured phase profiles $f(x, y)$. It follows that there are two interferometric conditions. First, the presence of a translational offset (Δx) between the object and reference

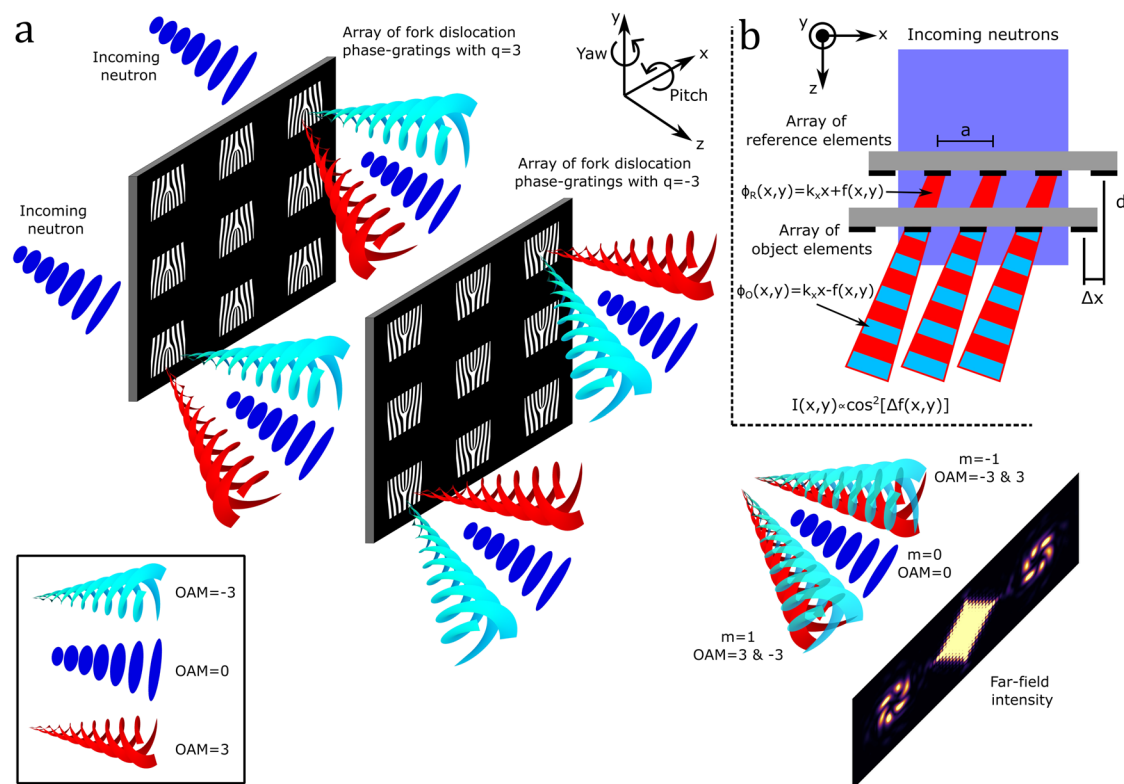


Fig. 1 | SANS interferometry with OAM states. **a** Pictorial depiction of the implemented SANS interferometry with orbital angular momentum (OAM) states. Ref. 25 showed that a single array of fork-dislocation phase gratings prepares helical waves in the diffraction orders that carry well-defined OAM values and manifest doughnut-like intensity profiles. Here, to observe the transverse phase profile of these helical waves, we create a coherent superposition between ℓ and $-\ell$ OAM states. Note that we have neglected the higher order interference as the direct beam is orders of magnitude brighter than the diffraction orders. **b** The general idea behind the SANS interferometry technique is to observe the phase profile of a

structured neutron beam with non-trivial propagation characteristics. We consider an incoming neutron with wave vector k_0 and two arrays with periodicity a and separation distance d . The array of reference beams needs to spatially overlap the array of object beams in order to interfere with the camera. Therefore, the amplitude of the reference beams needs to diffract similarly to the object beams. One straightforward approach to achieve this is by ensuring that the phase profile of the reference beams $\phi_R(x, y)$ and the object beams $\phi_O(x, y)$ possess a matching carrier wave vector k_x , complementary structured phase profiles $f(x, y)$, and enforcing a translational shift Δx that ensures overlap (See Eq. (1)).

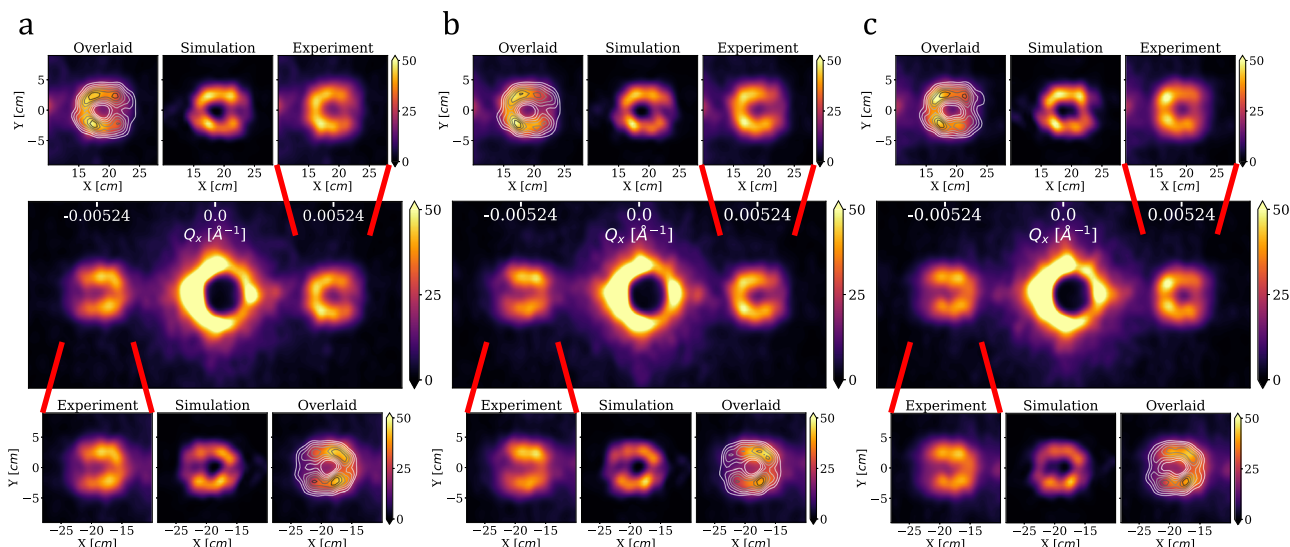


Fig. 2 | Neutron helical wave interference. The observed petal-structure signatures of neutron helical wave interference in the first diffraction orders as the pitch and yaw of the double-sided arrays of fork-dislocation phase-gratings were varied. **a** We find agreement for a simulation that considers a transverse coherence length of $\sigma_{\perp} = 3 \mu\text{m}$ and translational offsets between the two arrays of $x_i = 0$,

$y_i = 800 \text{ nm}$. **b** The SANS image after increasing the pitch by $\approx 0.6 \text{ mrad}$ corresponds to an updated offset of $x_i = 0 \text{ nm}$, $y_i = 961 \text{ nm}$. **c** The profile following an additional increment in yaw by $\approx 0.5 \text{ mrad}$ corresponding to $x_i = -135 \text{ nm}$, $y_i = 961 \text{ nm}$. In this proof of principle experiment, the poor visibility is mainly attributed to the wavelength spread, as depicted in Fig. 3.

elements that ensures the reference and object beams are collinear:

$$\Delta x \approx d \cdot \tan(k_p/k_0) = d \cdot \tan(\lambda/p) \approx d\lambda/p, \quad (1)$$

where λ (k_0) is the neutron wavelength (wave vector), and p (k_p) is the periodicity (wave vector) of the object and reference elements. If Δx is greater than the array period a , then the effective translation becomes $\Delta x \bmod a$. Note that the highest contrast occurs for the case where the translational offset is a multiple of the array periodicity, $\Delta x = n \cdot a$ for some integer n . The second condition is that the transverse coherence length needs to be greater than Δx , as the interference is between the first diffraction orders of the incoming beam.

Experimental implementation

The silicon wafer sample with the double-sided arrays of fork-dislocation phase-gratings was mounted in a holder that was then placed on a manual tip-tilt stage with access to yaw ($\approx 2.9 \text{ mrad/rev}$) and pitch ($\approx 6.9 \text{ mrad/rev}$) degrees of rotation. The experiment consisted of measuring the SANS intensity profile for 90 min as the yaw and pitch were systematically varied by $1/6 \text{ rev}$ and $1/12 \text{ rev}$, respectively. Given the neutron wavelength of 12 \AA , the phase-grating period $p = 120 \text{ nm}$, and the thickness of the wafer $d = 280 \mu\text{m}$, we can determine the optimal translational offset (see Eq. (1)) to be $\Delta x \approx 2.8 \mu\text{m}$; which from the fact that the period of the array is $2 \mu\text{m}$ reduces to $\Delta x \approx 0.8 \mu\text{m}$ or a wafer rotation angle of $\approx 3 \text{ mrad}$.

To determine the behavior of the interference pattern at the camera we analyze the propagation of the neutron wave function through the object and reference elements given the experimental parameters. Let us consider the wave function of a neutron wave packet after passing through the first array:

$$\psi_i(x, y) = \frac{1}{\sigma_{\perp} \sqrt{\pi}} e^{-\frac{x^2 + y^2}{2\sigma_{\perp}^2}} e^{iNb_c \lambda h F_3[x, y]}, \quad (2)$$

where $\sigma_x = \sigma_y = \sigma_{\perp}$ is the neutron transverse coherence length, Nb_c is the scattering length density of the sample material, λ is the neutron wavelength, h is the height of the grating structures, and $F_q(x, y)$ is the profile of an array of fork-dislocation phase-gratings whose individual

profiles are given by:

$$\frac{1}{2} \text{sgn} \left(\sin \left[\frac{2\pi}{p} x + q \tan^{-1}(y/x) \right] \right) + \frac{1}{2}, \quad (3)$$

where p is the grating period and q is its topological charge. Note that for $F_q(x, y)$ in our simulations we considered the SEM profiles found in the Supplementary Material of ref. 25. The wave function is then propagated a distance of $280 \mu\text{m}$ as per the wafer thickness, at which point the phase profile corresponding to the second array is added: $Nb_c \lambda h F_{-3}[x - x_i, y - y_i]$, where $\{x_i, y_i\}$ is the translational offset between the two arrays that results from the pitch and yaw increments. The intensity $I(x', y')$ at the camera is well approximated by:

$$I(x' \equiv k_x \lambda z, y' \equiv k_y \lambda z) = |FT\{\psi_f(x, y)\}|^2, \quad (4)$$

where $FT\{\}$ is the Fourier Transform, z is the distance from the wafer to the camera, and $\psi_f(x, y)$ is the wave function after the second array. To account for the experimental parameters that set the resolution of $\sigma_{Qx} \approx \sigma_{Qy} \approx 0.00016 \text{ \AA}^{-1}$, we add a low-pass filter with the corresponding cutoff frequency to the obtained intensity profile. This removes the diffraction signatures from the $2 \mu\text{m}$ periodicity of the arrays.

Figure 2 shows the observed petal-structure signatures of neutron helical wave interference in the first diffraction orders. Using $\sigma_{\perp} = 3 \mu\text{m}$ we find good agreement for Fig. 2a for $x_i = 0$, $y_i = 800 \text{ nm}$. Fig. 2b shows the SANS image after increasing the pitch by $\approx 0.6 \text{ mrad}$ and Fig. 2c shows the profile following an additional increment in yaw by $\approx 0.5 \text{ mrad}$. The simulated profiles are then determined by the addition of the corresponding translational offsets of $x_i = 0 \text{ nm}$, $y_i = 961 \text{ nm}$ for Fig. 2b, and $x_i = -135 \text{ nm}$, $y_i = 961 \text{ nm}$ for Fig. 2c.

Figure 3 shows how the petal-structure intensity profile is affected by array periodicity, the distance between the reference and object elements, phase shift between the two interfering OAM states, and wavelength distribution. Note that in Fig. 3, we consider the described experimental parameters but with the mentioned optimal case scenario of array period equaling the translational offset $a = \Delta x = 2.8 \mu\text{m}$.

Lastly, we can note that although our model considers the full diffraction spectra, the main contributing factors are the two

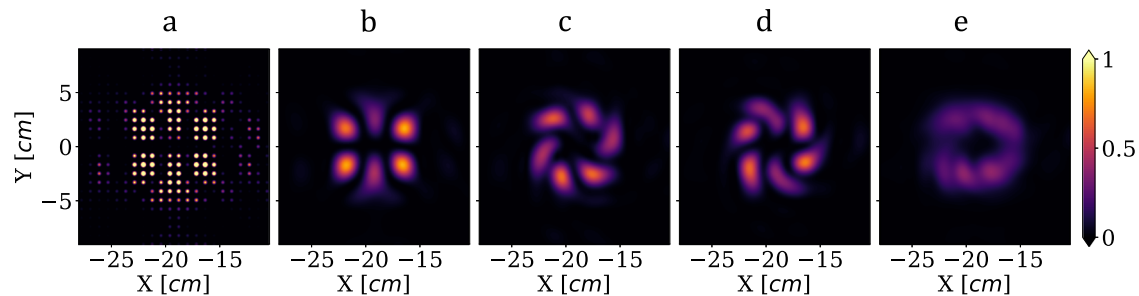


Fig. 3 | Modeling the effects of experimental parameters on the petal-structure interference. The effect of array structure, distance between the reference and object elements, phase shift between the two interfering OAM states, and wavelength distribution on the petal-structure intensity profile produced in the first diffraction order by the double-sided arrays of fork-dislocation phase gratings. **a** Considering an ideal coherent and monochromatic neutron beam incident on object and reference elements with negligible distance between them, one would be able to resolve the interference pattern that is both indicative of the OAM

interference and the two-dimensional array structure. **b** Removing the higher order frequencies corresponding to the two-dimensional array structure results in the OAM petal structure being emphasized. **c** Increasing the distance between the reference and object elements to the experimental value of 280 μm introduces a phase shift and propagation diffraction that manifests a winding structure in the interference pattern. **d** Adding to the object beams an additional OAM dependent π phase shift effectively rotates the petal pattern of **c**. **e** Increasing the wavelength distribution to the experimental $\Delta\lambda/\lambda \approx 0.13$ smears the interference pattern of **c**.

complementary OAM states, as shown in Fig. 1a. Taking note that each wavelength results in a displaced intensity profile at the camera as per the diffraction angle of $\approx \lambda/p$, it can be shown that for the considered parameters the superposition of OAM = -3 & 3 simulates almost identical petal-structure intensity profiles as shown in Figs. 2 and 3.

Discussion

We have introduced and demonstrated a novel NI technique for extracting phase information that is typically lost in SANS measurements. By preparing reference beams with complementary spatial phase profiles to that of the object beams, we observed the petal-structure signatures of neutron helical wave interference for the first time. With the growing number of neutron-imaging and -scattering user facilities worldwide^{43,44}, the demonstrated techniques are set to make a high impact in the next generation of neutron scattering studies. Furthermore, it is also possible that this approach could be extended to SAXS⁴⁵. Lastly, these methods can be extended to implementations with helical waves of atoms and molecules⁴⁶, which also rely on arrays of fork-dislocation gratings.

The employed neutron optics element, which was composed of an array of fork-dislocation phase gratings on both sides of a silicon wafer, adds an additional capability to the toolbox of structured neutron waves for the studies of helical features. Analogous to a $\pi/2$ spin flipper that prepares a coherent superposition of two orthogonal spin states, this element prepares a coherent superposition of two OAM states. Future experiments employing this element will study helical phase shifts from materials; for example, probing chiral skyrmion lattices to reveal scattering properties and phase information with SANS^{17,47}. Moreover, combining the coherent superposition of vortex states with Airy beams may provide a more attractive probe for chiral media that is non-diffracting^{48–52}.

There are several ways to improve the observed visibility of the presented helical wave interference. In this proof of principle experiment, the poor visibility is mainly attributed to the width of the wavelength distribution. Furthermore, mechanical drifts and ambient conditions, which typically are not a concern for SANS measurements of grating structures, can induce dephasing that degrades the visibility of the interference pattern. We can also note that as nanofabrication methods advance, it is expected that a much higher signal in the diffraction orders will become obtainable. For example, if amplitude-gratings or phase-grating with heights of 5 μm were feasible, then the intensity in the diffraction orders would be around a hundred times higher compared to this experiment that employed phase-grating

heights of 500 nm. The corresponding measuring time of < 1 min would enable a wide range of possibilities.

Methods

To aid in alignment, we employed double-sided nanofabrication methods. An array of fork-dislocation phase-gratings was fabricated on both sides of a silicon wafer where on one side there was a $q=3$ topology and the other side possessed $q=-3$, which results in them being 180° relative to each other. The arrays covered a 0.5 cm by 0.5 cm area and consisted of 6, 250, 000 individual $1\ \mu\text{m}$ by $1\ \mu\text{m}$ fork-dislocation phase-gratings, where each one possessed a period of 120 nm, height 500 nm, and was separated by $1\ \mu\text{m}$ on each side from the other fork-dislocation phase-gratings. The fab procedure for a single array can be found in the Supplementary Material of ref. 25. After fabricating the front side of the wafer, it was spun with a thick PMMA to protect the fabricated gratings for future steps. Using the back-side alignment feature at a maskless aligner (MLA 150, Heidelberg Instrument), cross-shape marks were placed on the other face of the wafer via the e-beam evaporation and lift-off techniques (Cr/Au 20/100 nm). The back-side alignment at MLA has an alignment accuracy of better than $1\ \mu\text{m}$. Based on these alignment marks, the second array of gratings was fabricated on the other face of the wafer.

A preliminary study was done at the SANS-1 beamline at the Paul Scherrer Institute⁵³, as a result of which an improved setup was devised and implemented at the GP-SANS beamline at the High Flux Isotope Reactor at Oak Ridge National Laboratory⁵⁴. The experimental parameters were the same as those in ref. 25, which described the observation of neutron helical waves. The double-sided wafer was placed inside a rotation mount which was placed 17.8 m away from a 20-mm diameter source aperture. A 4-mm diameter sample aperture was placed right in front of the sample. The distance from the sample to the camera was 19 m, and the camera size spans an area of $\approx 1\ \text{m}^2$ with each pixel being $\approx 5.5\ \text{mm}$ by $4.3\ \text{mm}$ in size. The wavelength distribution was triangular with $\Delta\lambda/\lambda \approx 0.13$, where $\Delta\lambda$ is the FWHM and the central wavelength is 12 \AA , and the standard deviation of the resolution distribution was estimated to be $\sigma_{Q_x} \approx \sigma_{Q_y} \approx 0.00016\ \text{\AA}^{-1}$. The neutron wavelength is selected by a turbine-like velocity selector, which eliminates the fractional λ contributions that are present when a monochromator crystal is used.

An empty beam scan without a sample and a background scan for a plain silicon wafer of equivalent size and thickness were collected. These measurements were used to take into account the factors that contribute to losses in intensity and increased background scattering

noise. The final SANS data was passed through a low-pass filter to remove the Poissonian noise that varies from pixel to pixel.

Data availability

All experimental data is available in the following public git repository: https://git.uwaterloo.ca/oalailey/sans_interferometry_nat_comm.

Code availability

All code to perform simulations is available in the following public git repository: https://git.uwaterloo.ca/oalailey/sans_interferometry_nat_comm.

References

- Schmitt, J. et al. Mesoporous silica formation mechanisms probed using combined spin-echo modulated small-angle neutron scattering (semsans) and small-angle neutron scattering (sans). *ACS Appl. Mater. Interfaces* **12**, 28461–28473 (2020).
- Perera, S. M. et al. Small-angle neutron scattering reveals energy landscape for rhodopsin photoactivation. *J. Phys. Chem. Lett.* **9**, 7064–7071 (2018).
- Lai, S. Y. et al. Silicon nanoparticle ensembles for lithium-ion batteries elucidated by small-angle neutron scattering. *ACS Appl. Energy Mater.* **2**, 3220–3227 (2019).
- Heller, W. T. Small-angle neutron scattering study of a phosphatidylcholine–phosphatidylethanolamine mixture. *ACS Omega* **8**, 33755–33762 (2023).
- Draper, E. R. et al. Using small-angle scattering and contrast matching to understand molecular packing in low molecular weight gels. *Matter* **2**, 764–778 (2020).
- Heller, W. T. A small-angle neutron scattering study of the physical mechanism that drives the action of a viral fusion peptide. *Chem. Phys. Lipids* **234**, 105022 (2021).
- Allen, A. J. Selected advances in small-angle scattering and applications they serve in manufacturing, energy and climate change. *J. Appl. Crystallogr.* **56**, 787–800 (2023).
- Fuhrman, W. et al. Interaction driven subgap spin exciton in the Kondo insulator SmB_6 . *Phys. Rev. Lett.* **114**, 036401 (2015).
- Qian, F. et al. New magnetic phase of the chiral skyrmion material Cu_2OSeO_3 . *Sci. Adv.* **4**, eaat7323 (2018).
- Dewhurst, C. et al. Néel-type skyrmion lattice with confined orientation in the polar magnetic semiconductor GaV_4S_8 . *Nat. Mater.* **14**, 1116–1122 (2015).
- Nagaosa, N. & Tokura, Y. Topological properties and dynamics of magnetic skyrmions. *Nat. Nanotechnol.* **8**, 899–911 (2013).
- Mühlbauer, S. et al. Magnetic small-angle neutron scattering. *Rev. Mod. Phys.* **91**, 015004 (2019).
- Schmatz, W., Springer, T., Schelten, J. T. & Ibel, K. Neutron small-angle scattering: experimental techniques and applications. *J. Appl. Crystallogr.* **7**, 96–116 (1974).
- Jeffries, C. M. et al. Small-angle X-ray and neutron scattering. *Nat. Rev. Methods Prim.* **1**, 70 (2021).
- Hollamby, M. J. Practical applications of small-angle neutron scattering. *Phys. Chem. Chem. Phys.* **15**, 10566–10579 (2013).
- Heacock, B. et al. Neutron sub-micrometre tomography from scattering data. *IUCr J* **7**, 893–900 (2020).
- Henderson, M. et al. Three-dimensional neutron far-field tomography of a bulk skyrmion lattice. *Nat. Phys.* **19**, 1617–1623 (2023).
- Clark, C. W. et al. Controlling neutron orbital angular momentum. *Nature* **525**, 504–506 (2015).
- Sarenac, D. et al. Holography with a neutron interferometer. *Opt. express* **24**, 22528–22535 (2016).
- Sarenac, D. et al. Generation and detection of spin-orbit coupled neutron beams. *Proc. Natl. Acad. Sci.* **116**, 20328–20332 (2019).
- Geerits, N., Lemmel, H., Berger, A.-S. & Sponar, S. Phase vortex lattices in neutron interferometry. *Commun. Phys.* **6**, 209 (2023).
- Sarenac, D. et al. Methods for preparation and detection of neutron spin-orbit states. *N. J. Phys.* **20**, 103012 (2018).
- Nsofini, J. et al. Spin-orbit states of neutron wave packets. *Phys. Rev. A* **94**, 013605 (2016).
- Jach, T. & Vinson, J. Method for the definitive detection of orbital angular momentum states in neutrons by spin-polarized He-3 . *Phys. Rev. C* **105**, L061601 (2022).
- Sarenac, D. et al. Experimental realization of neutron helical waves. *Sci. Adv.* **8**, eadd2002 (2022).
- Le Thien, Q., McKay, S., Pynn, R. & Ortiz, G. Spin-textured neutron beams with orbital angular momentum. *Phys. Rev. B* **107**, 134403 (2023).
- Larocque, H., Kaminer, I., Grillo, V., Boyd, R. W. & Karimi, E. Twisting neutrons may reveal their internal structure. *Nat. Phys.* **14**, 1 (2018).
- Sherwin, J. A. Scattering of slow twisted neutrons by ortho- and parahydrogen. *Phys. Lett. A* **437**, 128102 (2022).
- Afanasev, A., Karlovets, D. & Serbo, V. Elastic scattering of twisted neutrons by nuclei. *Phys. Rev. C* **103**, 054612 (2021).
- Afanasev, A. V., Karlovets, D. & Serbo, V. Schwinger scattering of twisted neutrons by nuclei. *Phys. Rev. C* **100**, 051601 (2019).
- Rubinsztein-Dunlop, H. et al. Roadmap on structured light. *J. Opt.* **19**, 013001 (2016).
- Bliokh, K. Y. et al. Roadmap on structured waves. *J. Opt.* **25**, 103001 (2023).
- Ivanov, I. P. Promises and challenges of high-energy vortex states collisions. *Prog. Part. Nucl. Phys.* **127**, 103987 (2022).
- Chen, J., Wan, C. & Zhan, Q. Engineering photonic angular momentum with structured light: a review. *Adv. Photonics* **3**, 064001 (2021).
- Ni, J. et al. Multidimensional phase singularities in nanophotonics. *Science* **374**, eabj0039 (2021).
- Allen, L., Beijersbergen, M. W., Spreeuw, R. J. C. & Woerdman, J. P. Orbital angular momentum of light and the transformation of Laguerre-Gaussian laser modes. *Phys. Rev. A* **45**, 8185–8189 (1992).
- Bazhenov, V. I., Vasnetsov, M. V. & Soskin, M. S. Laser beams with wave front screw dislocations. *Pisma v. Zh. Eksperimentalnoi i Teoreticheskoi Fiz.* **52**, 1037–1039 (1990).
- Berry, M. Optical vortices evolving from helicoidal integer and fractional phase steps. *J. Opt. A: Pure Appl. Opt.* **6**, 259 (2004).
- Rauch, H. & Werner, S. A. Neutron interferometry: lessons in experimental quantum mechanics, wave-particle duality, and entanglement, vol. 12 (Oxford University Press; 2 edition, 2015).
- Leith, E. N. & Upatnieks, J. Wavefront reconstruction with continuous-tone objects*. *J. Opt. Soc. Am.* **53**, 1377–1381 (1963).
- Gähler, R., Felber, J., Mezei, F. & Golub, R. Erratum: Space-time approach to scattering from many-body system. *Phys. Rev. A* **58**, 4249–4249 (1998).
- Fickler, R., Krenn, M., Lapkiewicz, R., Ramelow, S. & Zeilinger, A. Real-time imaging of quantum entanglement. *Sci. Rep.* **3**, 1914 (2013).
- Garoby, R. et al. Progress on the ess project construction. *Proceedings of IPAC* (2017).
- Alarcon, R. et al. Fundamental neutron physics: a white paper on progress and prospects in the us. *arXiv* <https://arxiv.org/abs/2308.09059> (2023).
- Woods, J. S. et al. Switchable x-ray orbital angular momentum from an artificial spin ice. *Phys. Rev. Lett.* **126**, 117201 (2021).
- Luski, A. et al. Vortex beams of atoms and molecules. *Science* **373**, 1105–1109 (2021).
- Henderson, M. E. et al. Characterization of a disordered above room temperature skyrmion material $\text{Co}_8\text{Zn}_8\text{Mn}_4$. *Materials* **14**, 4689 (2021).
- Karlovets, D. V. Gaussian and airy wave packets of massive particles with orbital angular momentum. *Phys. Rev. A* **91**, 013847 (2015).

49. Mazilu, M., Baumgartl, J., Čižmár, T. & Dholakia, K. Accelerating vortices in airy beams. Forbes, A. & Lizotte, T. E. (eds.) *Laser Beam Shaping X*, vol. 7430, 74300C. International Society for Optics and Photonics (SPIE, 2009).
50. Dai, H. T., Liu, Y. J., Luo, D. & Sun, X. W. Propagation dynamics of an optical vortex imposed on an airy beam. *Opt. Lett.* **35**, 4075–4077 (2010).
51. Dai, H. T., Liu, Y. J., Luo, D. & Sun, X. W. Propagation properties of an optical vortex carried by an airy beam: experimental implementation. *Opt. Lett.* **36**, 1617–1619 (2011).
52. Liu, X. & Zhao, D. Propagation of a vortex airy beam in chiral medium. *Opt. Commun.* **321**, 6–10 (2014).
53. Kohlbrecher, J. & Wagner, W. The new sans instrument at the swiss spallation source SINQ. *J. Appl. Crystallogr.* **33**, 804–806 (2000).
54. Wignall, G. D. et al. The 40 m general purpose small-angle neutron scattering instrument at Oak Ridge National Laboratory. *J. Appl. Crystallogr.* **45**, 990–998 (2012).

Acknowledgements

This work was supported by the Canadian Excellence Research Chairs (CERC) program, the Natural Sciences and Engineering Research Council of Canada (NSERC), the Canada First Research Excellence Fund (CFREF), and the US Department of Energy, Office of Nuclear Physics, under Interagency Agreement 89243019SSC000025 (M.G.H.). This work was also supported by the DOE Office of Science, Office of Basic Energy Sciences, in the program “Quantum Horizons: QIS Research and Innovation for Nuclear Science” through grant DE-SC0023695 (D.A.P. and O.L.). A portion of this research used resources at the High Flux Isotope Reactor, a DOE Office of Science User Facility operated by the Oak Ridge National Laboratory. The beam time was allocated to GP-SANS (CG2) on proposal number IPTS-30325. This work is based partly on experiments performed at the Swiss spallation neutron source SINQ, Paul Scherrer Institute, Villigen, Switzerland. Certain trade names and company products are mentioned in the text or identified in an illustration in order to adequately specify the experimental procedure and equipment used. In no case does such identification imply recommendation or endorsement by the National Institute of Standards and Technology, nor does it imply that the products are necessarily the best available for the purpose.

Author contributions

D.S. and D.A.P. conceived the method. H.E. fabricated the double-sided array. D.S., D.A.P., M.E.H., L.D.-S., J.S.W., and K.Z. performed the experiment. O.L., D.S., and D.A.P. developed the model for simulations

and experimental analysis. D.S., M.E.H., H.E., C.W.C., D.G.C., L.D.-S., M.G.H., O.L., J.S.W., K.Z., and D.A.P. contributed to data analysis and manuscript write-up.

Competing interests

D.S. and D.A.P. are inventors on a patent related to this work filed by Incoherent Vision Inc., US Patent App. 17/300,329. The remaining authors declare no competing interests.

Additional information

Supplementary information The online version contains supplementary material available at <https://doi.org/10.1038/s41467-024-54991-8>.

Correspondence and requests for materials should be addressed to Dusan Sarenac or Dmitry A. Pushin.

Peer review information *Nature Communications* thanks Henry Fischer and the other, anonymous, reviewer(s) for their contribution to the peer review of this work. A peer review file is available.

Reprints and permissions information is available at <http://www.nature.com/reprints>

Publisher’s note Springer Nature remains neutral with regard to jurisdictional claims in published maps and institutional affiliations.

Open Access This article is licensed under a Creative Commons Attribution-NonCommercial-NoDerivatives 4.0 International License, which permits any non-commercial use, sharing, distribution and reproduction in any medium or format, as long as you give appropriate credit to the original author(s) and the source, provide a link to the Creative Commons licence, and indicate if you modified the licensed material. You do not have permission under this licence to share adapted material derived from this article or parts of it. The images or other third party material in this article are included in the article’s Creative Commons licence, unless indicated otherwise in a credit line to the material. If material is not included in the article’s Creative Commons licence and your intended use is not permitted by statutory regulation or exceeds the permitted use, you will need to obtain permission directly from the copyright holder. To view a copy of this licence, visit <http://creativecommons.org/licenses/by-nc-nd/4.0/>.

© The Author(s) 2024